# Banana peel biomass-derived carbon and nitrogen-doped quantum dot/UiO-66 hybrid nanocomposites for high-performance asymmetric supercapacitors

# Banana Peel Biomass-Derived Carbon and Nitrogen-Doped Quantum Dot/UiO-66 Hybrid Nanocomposites for High-Performance Asymmetric Supercapacitors

Nur Irdina Atasya Abu Hassanisazin[a], Harivalagan Siva Kumar[a], Siti Aisyah Shamsudin[a*], Fatin Saiha Omar[a], Theodore Azemtsop Manfo[b]

[a]Department of Physics, Faculty of Science and Technology, Universiti Kebangsaan Malaysia (UKM), 43600 Bangi, Selangor, Malaysia

[b]Department of Electrical Engineering and Energy Technology, School of Technology and Innovations, Wolffintie 32, Vaasa 65200, Finland

*Corresponding author: aisyah@ukm.edu.my, Tel: +603-8921 3343

## Abstract

Supercapacitors are promising energy storage devices, yet their wide application is limited by low energy density. Similarly, UiO-66, a zirconium-based metal–organic framework (MOF), possesses a high surface area but suffers from poor electrical conductivity. To overcome these limitations, nitrogen-doped carbon quantum dots (NCQDs) derived from banana peel biomass were synthesised via a green hydrothermal approach and embedded into the UiO-66 framework. This integration preserved the MOF's structural integrity while the introduced nitrogen functionalities enhanced interfacial interactions, electrical conductivity and electron-transfer pathways. Consequently, the UiO-66/NCQDs hybrid exhibited lower charge-transfer resistance and superior redox activity compared with pristine UiO-66 and UiO-66/CQDs. In an asymmetric supercapacitor assembled with activated carbon, the hybrid electrode delivered a specific energy of 30.32 Wh $kg^{-1}$ at a power density of 2449.38 W $kg^{-1}$, retaining 93.45% of its capacitance after 4000 cycles. These findings demonstrate a sustainable strategy for engineering high-performance, biomass-derived MOF/QD energy storage devices.

Keywords: UiO-66 metal-organic framework, nitrogen-doped carbon quantum dots, biomass waste, hybrid nanocomposite electrode, asymmetric supercapacitor

## Highlights

- Banana peel–derived NCQDs integrated into UiO-66 framework
- Nitrogen groups enhance pore confinement and conductivity
- Denser packing with stronger H-bonding and Zr–O coordination
- N-doping lowers ESR and accelerates redox kinetics in UiO-66/NCQDs
- UiO-66/NCQDs//AC device delivers an exceptionally high 2.45 kW $kg^{-1}$ power

## Graphical Abstract

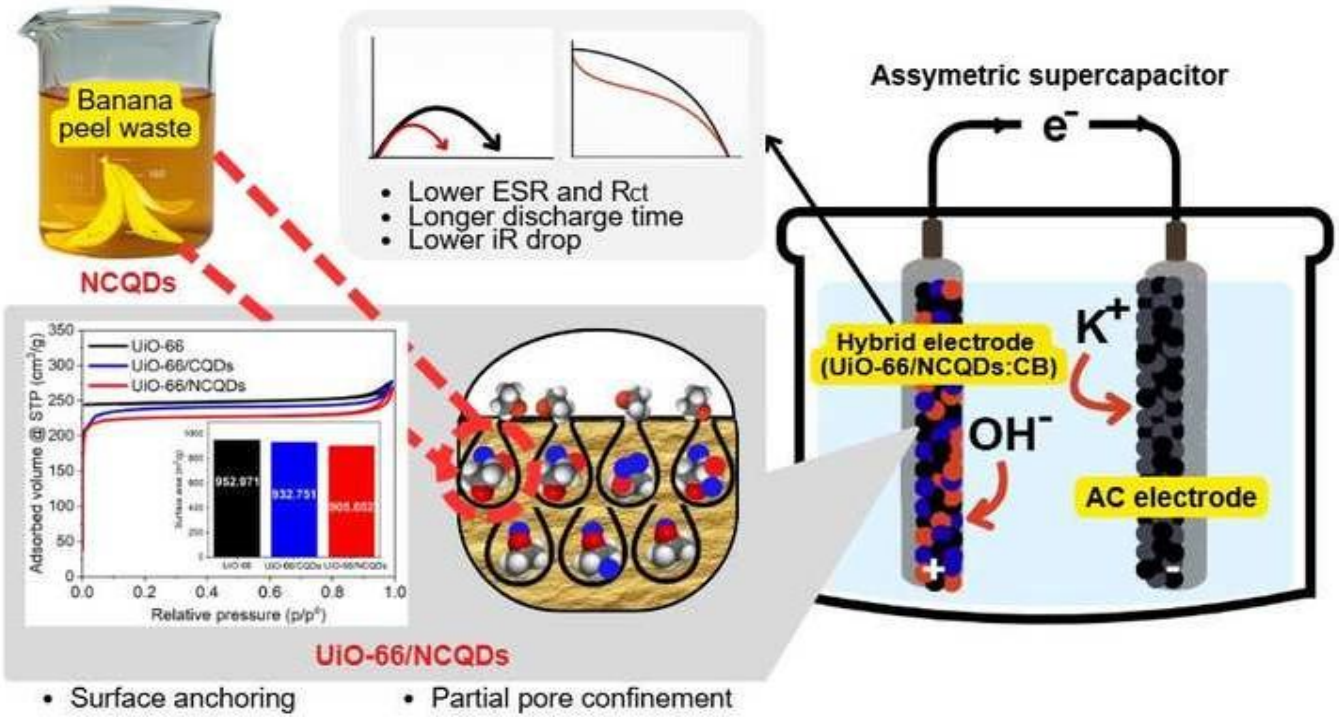
Banana peel waste
NCQDs
• Lower ESR and Rct
• Longer discharge time
• Lower iR drop
Assymetric supercapacitor
e-
Hybrid electrode (UiO-66/NCQDs:CB)
K+
OH-
AC electrode
UiO-66
UiO-66/CQDs
UiO-66/NCQDs
Adsorbed volume @ STP (cm3/g)
Relative pressure (p/p°)
952.871
932.751
UiO-66/NCQDs
• Surface anchoring
• Partial pore confinement

## 1.0 Introduction

The rapid growth of the global energy sector is a major driver of carbon emissions; thus, a transition to sustainable, low-carbon energy technologies is essential. Although renewable energy sources, such as solar and wind, have advanced notably, their intermittent nature threatens grid reliability. Hence, there is a need for advanced energy storage systems that can ensure stable power delivery [1]. Conventional electrochemical energy storage devices, including batteries and supercapacitors (SCs), are limited by their intrinsic trade-offs. SCs offer high power density, rapid charge-discharge capabilities, and long cycle life, but their low energy density restricts large-scale applications. By contrast, batteries offer higher energy densities but suffer from slow kinetics, limited cycling stability, and safety issues [2]. Hybrid configurations have been developed to bridge these limitations; these include, asymmetric supercapacitors (ASCs), which combine electric double-layer capacitance (EDLC) with faradaic redox mechanisms to extend the cell-operating voltage window and combine the advantages of both systems [3].

Beyond device engineering, finding sustainable electrode materials is key to improving performance. Biomass valorisation has emerged as an eco-friendly route for converting agricultural waste into functional carbon nanostructures, while aligning with circular economy goals. In Malaysia, banana peels are a major food waste stream that contributes to methane emissions in landfills; thus, recycling this biomass into carbon quantum dots (CQDs) shows potential for energy applications [4]. Although biomass-derived CQDs possess tuneable properties and abundant surface functional groups, pristine CQDs are prone to self-aggregation and exhibit poor electrical conductivity, severely limiting their electrochemical utilisation [5]. Heteroatom doping, particularly with nitrogen, resolves this problem by accelerating electron transfer and enhancing pseudocapacitive redox activity compared to undoped counterparts [6], [7]. However, there have been few studies on the systematic integration of biomass-derived nitrogen-doped CQDs (NCQDs) into UiO-66 metal-organic framework (MOF)-based electrode architectures for electrochemical energy storage.

Metal-organic frameworks (MOFs) are highly promising for energy storage because of their ultrahigh surface area and tuneable pore distributions [8], [9]. Among typical MOFs, zirconium (Zr)-based UiO-66, composed of $Zr_6O_4(OH)_4$ nodes and terephthalate (BDC) linkers, is renowned for its exceptional thermal and chemical stability. Although pristine UiO-66 suffers from intrinsically poor electrical conductivity [10], it was selected as the host matrix in this study because of its unique thermodynamic stability, arising from strong Zr-O bond coordination, alongside its rigid, well-defined pore structure. Unlike other MOFs that easily degrade or undergo framework collapse when exposed to harsh aqueous electrolytes during long-term testing, the Zr framework of UiO-66 maintains its structural integrity while providing stable, accessible pores to anchor conductive guest materials.

Conductive carbon nanomaterials have been widely explored as guest components within MOF architectures to overcome the conductivity limitations of UiO-66 without the excessive

incorporation of conductive additives, which often block pores and restrict ion diffusion. Over the past 3–5 years, research has focused on enhancing the intrinsic conductivity of MOFs through hybridisation with various carbonaceous nanomaterials, including carbon nanotubes, graphene QDs, and synthetic carbon dots [11], [12]. Although these approaches have improved specific capacitance, many MOF/carbon hybrid systems continue to suffer from carbon agglomeration, external pore blockage, and inefficient charge-transfer pathways, which limit ion accessibility, power capability, and long-term electrochemical performance. These challenges highlight the need for conductive nanocarbon modifiers that can be homogeneously integrated within MOF architectures while preserving the intrinsic porosity and structural integrity of the frameworks.

This work addresses these challenges by incorporating banana peel waste-derived NCQDs into the UiO-66 framework to produce sustainable hybrid nanocomposite electrodes. This approach represents an eco-friendly and cost-effective utilisation of agricultural waste precursors. Furthermore, the nitrogen-rich surface functionalities of the biomass-derived NCQDs promote stronger host–guest interactions with UiO-66, suppress carbon aggregation, and establish continuous electron-transfer pathways while preserving the intrinsic porosity of the framework. Building upon our previous work, in which we optimised the synthesis and physicochemical properties of CQDs and NCQDs [13], we extend their application to the production of UiO-66-based asymmetric supercapacitor electrodes. Nitrogen species, such as pyridinic and pyrrolic nitrogen, can contribute additional electroactive sites and enhance electrolyte accessibility, promoting synergistic electric double-layer capacitance (EDLC) and faradaic charge-storage processes. Therefore, this study aimed to develop a sustainable UiO-66/NCQD hybrid electrode and systematically investigate the host–guest interaction mechanisms, structural evolution, and charge-storage behaviour governing its electrochemical performance. The goal was to provide deeper insight into the design of high-performance MOF/QD hybrid electrodes for next-generation supercapacitors.

## 2.0 Experimental

### 2.1 Materials

UiO-66 (Zr-MOF) was purchased from Sigma-Aldrich (Petaling Jaya, Malaysia). Banana peel was used as a precursor for the synthesis of CQDs and NCQDs, with ethylenediamine ($C_2H_8N_2$, Sigma-Aldrich, Malaysia) as the nitrogen source. Activated carbon (AC) and carbon black (CB) (Alfa Aesar) were used as conductive additives. Polyvinylidene fluoride *(PVDF)* and *N*-methyl-2-pyrrolidone (NMP) from Sigma-Aldrich was utilized as the binder and solvent, respectively, for electrode slurry preparation. All chemicals were of analytical grade and were used without further purification. Deionised (DI) water was employed in all the experiments.

### 2.2 Synthesis of Carbon Quantum Dots (CQDs) and Nitrogen-Doped CQDs (NCQDs)

CQDs and NCQDs were synthesised via a hydrothermal method. For NCQDs, 0.06 g of banana peel-derived carbon precursor was dispersed in 80 mL of deionised (DI) water, followed by the

addition of 1 mL ethylenediamine as the nitrogen source. The nitrogen-doping condition was selected based on the optimised composition established in our previous study [13], in which NCQDs-1.25% exhibited the highest colloidal stability, fluorescence intensity, and particle size homogeneity. The suspension was transferred into a Teflon-lined stainless-steel autoclave and heated at 200 °C for 24 h. The resulting brown solution was subsequently filtered through a 0.22 μm syringe-mounted microfilter to remove residual particulates. The purified product exhibited a yellowish fluorescence under ambient light. CQDs were prepared using the same procedure without the addition of ethylenediamine, as reported previously [13]. All samples were synthesised independently under identical conditions, and the resulting dispersions were used directly for hybrid nanocomposite fabrication to ensure reproducibility.

### 2.3 Preparation of UiO-66/CQDs and UiO-66/NCQDs Hybrid Nanocomposites

UiO-66/CQDs and UiO-66/NCQDs nanocomposites were prepared via a green embedding method. Briefly, 40 mL CQDs or optimised NCQDs-1.25% dispersion was combined with 0.2 g of UiO-66 and stirred for 24 h at room temperature, followed by sonication for 15 min to ensure a homogeneous dispersion and effective interfacial interaction. The resulting suspension was filtered and washed sequentially three times with acetone and deionised water to remove unbound species. The NCQD loading in the UiO-66 framework was estimated by mass balance, using the difference between the initial UiO-66 mass (0.200 g) and the recovered dried UiO-66/NCQDs composite mass (0.211 g) after filtration, washing and drying. The NCQDs loading was estimated to be approximately 5.2 wt%. Fig. 1 (a-b) shows the schematic representation of the synthesis of NCQDs and the hybrid nanocomposite formation process.

### 2.4 Electrode Fabrication

As-prepared and modified MOFs were employed as active materials. As shown in Fig. 1 (c), the hybrid UiO-66/NCQDs nanocomposite was mixed with conductive CB and polyvinylidene difluoride (PVDF) at mass fractions of 75, 15 and 10 wt%, respectively. The resulting slurry was uniformly coated onto nickel foam (1 × 1 $cm^2$, 2 mm thickness), which served as both the current collector and substrate for the active material. The mass loading of the active material was approximately 6 mg $cm^{-2}$. The coated electrodes were subsequently dried at 90 ºC for 12 h to completely remove the solvent.

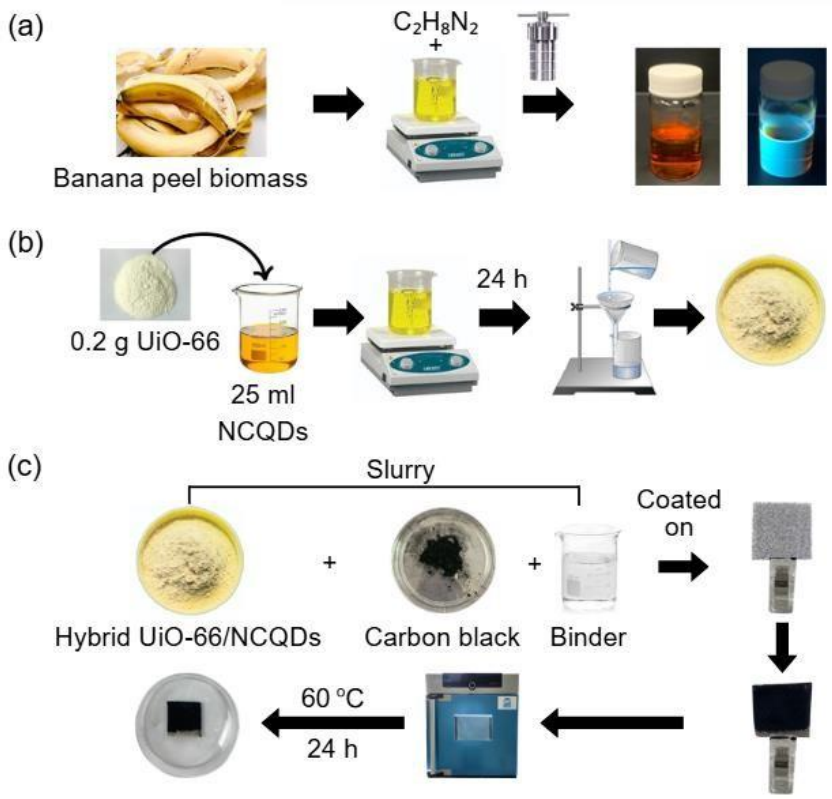


Fig. 1 Schematic illustration of the (a) the hydrothermal synthesis of NCQDs from banana peel biomass, (b) the formation of UiO-66/NCQD hybrid nanocomposites via a green embedding method and (c) fabrication process for UiO-66/CQDs and UiO-66/NCQDs hybrid electrodes

## 3.0 Characterization Techniques

### 3.1 Structural, Morphological, and Chemical Characterization

The morphology and particle size of UiO-66 and its hybrid nanocomposites were characterized by field-emission scanning electron microscopy (FESEM; Zeiss Supra 55VP, Germany) and transmission electron microscopy (TEM; Talos L120C, FEI, Netherlands) operated at 120 kV. Additional characterisation of the synthesised NCQDs, including morphological, optical, and surface analyses, was performed using TEM, Fourier transform infrared (FTIR; PerkinElmer Spectrum 400, USA) spectroscopy, zeta potential measurements, UV–Vis absorption spectroscopy, and photoluminescence spectroscopy. The results are provided in the Supplementary Information (Figs. S2-S6). Crystallinity and phase structure were analysed using X-ray diffraction (XRD; Bruker D8 Advance, Cu Kα, λ = 1.5418 Å) over 2θ = 0–70° at a scanning rate of 150 $min^{-1}$. The average crystallite size (D) was calculated using the Scherrer equation, according to Eq. (1) [14].

$$D = \frac{K\lambda}{\beta \cos\theta} \qquad (1)$$

Where $K$ is the Scherrer constant (0.89), $\lambda$ is the X-ray wavelength (1.5418 Å), β is the full width at half maximum (FWHM) in radians, and $\theta$ is the Bragg angle.

FTIR spectroscopy was employed to identify functional groups over 700–4000 $cm^{-1}$. Proton nuclear magnetic resonance ($^1H$ NMR; Avance III HD 400 MHz, Bruker, USA) was performed in $D_2O$ at 28 °C to verify the successful incorporation of CQDs and NCQDs into UiO-66. Nitrogen adsorption–desorption isotherms were measured at 77 K (Micromeritics Tristar II Plus 3030KR), and the specific surface area and pore size distribution were calculated using the Brunauer–Emmett–Teller (BET) and Barrett–Joyner–Halenda (BJH) methods, respectively.

### 3.2 Electrochemical measurements

The electrochemical performance of pristine UiO-66 and its hybrids (UiO-66/CQDs and UiO-66/NCQDs) was evaluated via cyclic voltammetry (CV), galvanostatic charge–discharge (GCD), and electrochemical impedance spectroscopy (EIS) using an Autolab PGSTAT302N (Metrohm).

In the three-electrode configuration (Fig. 2(a)), nickel foam coated with the active material served as the working electrode, the Hg/HgO electrode acted as the reference, and the platinum plate functioned as the counter electrode. Cyclic voltammetry (CV) was performed within a potential window of 0–0.6 V at scan rates of 3–50 mV $s^{-1}$, GCD was conducted at current densities of 1.0–5.0 A $g^{-1}$. Three independently prepared electrodes were fabricated for each sample and tested under identical electrochemical conditions to assess reproducibility. The average specific capacitance values and corresponding standard deviations are presented in Fig. S1 and Table S1 of the Supporting Information. Electrochemical impedance spectroscopy (EIS) measurements were performed over a frequency range of 0.01 Hz–100 kHz with an AC amplitude of 10 mV.

For the two-electrode full-cell configuration (Fig. 2(b)), UiO-66/NCQDs//AC electrodes were separated by a 25 μm Celgard polymer membrane and immersed in a 2 M KOH electrolyte. CV was conducted within potential windows of 0–1.0 to 2.0 V at scan rates of 3–50 mV $s^{-1}$. GCD was carried out within 0–1.8 V at 1.0–5.0 A $g^{-1}$. Cycling stability and the Ragone plot were derived from the GCD data.

The specific capacitance (C, F $g^{-1}$) of the electrodes was calculated from the discharge curves according to Eq. (2) [15].

$$C = \frac{I.\Delta t}{m.\Delta V} \qquad (2)$$

Where $I$ is the discharge current (A), $\Delta t$ is the discharge time (s), $m$ is the mass of active material in a single electrode (g), and $\Delta V$ is the potential window after IR drop (V).

Capacitive retention (%) after $N$ cycles was evaluated by comparing the specific capacitance at cycle $n$ with the initial cycle using Eq. (3).

$$Retention\ (\%) = \frac{C_n}{C_o}\ x\ 100 \qquad (3)$$

where $C_0$ and $C_n$ are the initial and nth-cycle capacitance values, respectively.

The specific energy (E, Wh $kg^{-1}$) and specific power (P, W $kg^{-1}$) for the Ragone plot were obtained using Eq. (4) and (5):

$$E = \frac{1}{2} C(\Delta V)^2 \; x \; \frac{1}{3.6} \qquad (4)$$

$$P = \frac{E \; x \; 3600}{\Delta t} \qquad (5)$$

Where $\Delta t$ (s) is the discharge time. The specific energy and specific power density of the UiO-66/NCQDs//AC asymmetric supercapacitor were calculated based on the total mass of both the positive and negative electrodes, including the active materials, conductive CB, and binder.

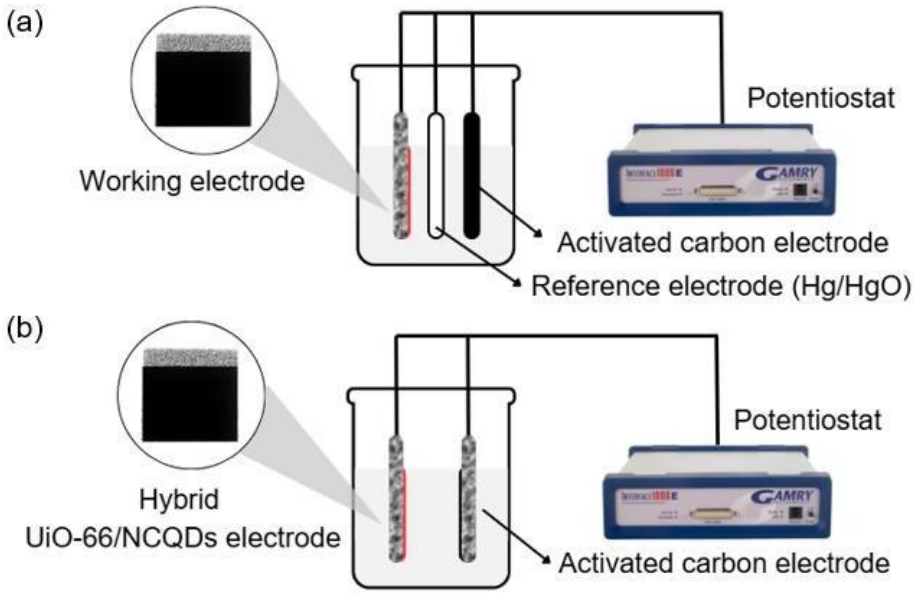


Fig. 2 Schematic of electrochemical measurement setups: (a) Three-electrode configuration with working electrode, reference electrode, and counter electrodes, and (b) two-electrode asymmetric device with separator and aqueous KOH electrolyte

## 4.0 Results and Discussion

### 4.1 Physicochemical Characterization

The morphologies of UiO-66 and its hybrid nanocomposites were determined by FESEM (Fig. 3a–c) and TEM (Fig. 3d-f). Pristine UiO-66 (Fig. 3a,d) displayed discrete polyhedral aggregates with smooth crystalline surfaces, consistent with well-crystallised Zr-based MOFs [16]. Upon incorporation of CQDs (Fig. 3b,e), the particles became more densely packed with sizes ranging from 5 to 7 nm. These surface features are due to the strong affinity of oxygenated functional groups on CQDs towards Zr metal clusters and organic linkers, leading to surface deposition and partial pore filling.

By contrast, the UiO-66/NCQDs hybrid (Fig. 3c,f) exhibited denser particle packing, slightly enlarged nanoparticles (6–6.5 nm), and finer hierarchical textures. These features can be

attributed to nitrogen-induced structural defects and enhanced interfacial interactions through hydrogen bonding and coordination with Zr nodes, which promote improved electron transport and interfacial electrical connectivity. TEM analysis of pristine NCQDs (Fig. S2) further confirmed the formation of uniformly distributed nanosized QDs, supporting their effective dispersion and interfacial integration within the UiO-66 framework. The improved homogeneity and stability of NCQDs, particularly at an optimised nitrogen content of 1.25%, led to more uniform surface coverage and reduced aggregation compared to CQDs [13], [17].

The $N_2$ adsorption–desorption isotherms at 77 K in Fig. 3(g) of UiO-66, UiO-66/CQDs, and UiO-66/NCQDs were analysed to assess the impact of QD incorporation on the porosity of the 3D UiO-66 framework. According to IUPAC classification, all three nanomaterials exhibited type I adsorption-desorption isotherms characteristic of microporous materials, as evidenced by the sharp uptake at low relative pressures without a hysteresis loop [18]. BET and BJH analyses revealed average pore widths of 6.86, 11.67, and 12.66 nm, with corresponding surface areas of 952.97, 932.75 and 905.85 $m^2/g$ for pristine UiO-66, UiO-66/CQDs and UiO-66/NCQDs, respectively (Table 1). The reduction in surface area following QD incorporation can be attributed to partial pore filling and surface deposition. This progressive decrease is due to the higher degree of nitrogen functionalisation on the NCQDs, that promoted strong interfacial interactions with the Zr oxide nodes of the framework. This enhanced affinity resulted in a more uniform and comprehensive surface coating along the pore walls, leading to greater internal pore confinement and localised volume restriction compared to unmodified CQDs [19], [20]. Notably, the high surface area of UiO-66 was largely preserved, with only marginal decreases of 2.12% and 4.94% for UiO-66/CQDs and UiO-66/NCQDs, respectively, indicating that the intrinsic porous framework remained intact. Such porosity retention is essential for pseudocapacitive charge storage, because it ensures abundant electrode–electrolyte interfacial contact and shorter ion diffusion pathways. The presence of conductive CQDs and NCQDs compensates for minor porosity losses by enhancing charge transport within the UiO-66 composite. This is advantageous because substantial porosity could impair electrochemical performance [21].

Table 1 BET surface area and BJH pore size distribution of pristine UiO-66, UiO-66/CQDs, and UiO-66/NCQDs

| Nanocomposite | BJH desorption average pore width (nm) | BET surface area ($m^2/g$) |
|---|---|---|
| UiO-66 | 6.87 | 952.97 |
| UiO-66/CQDs | 11.67 | 932.75 |
| UiO-66/NCQDs | 12.66 | 905.85 |

The XRD profile (Fig. 3(h)) confirmed that the 3D UiO-66/CQDs and UiO-66/NCQDs nanocomposites retained the UiO-66 crystalline topology, exhibiting diffraction peaks at $2\theta$ = 7.37°, 8.51°, and 25.71°, indexed to the (111), (002) and (006) planes, respectively. A slight decrease in crystallinity was observed, from 98.2% in pristine UiO-66 to 89.6% and 86.8% for UiO-66/CQDs and UiO-66/NCQDs, respectively. This decrease is due to the amorphous nature of

carbon dots, whose broad diffraction features overlap with those of UiO-66, slightly reducing their long-range order. The persistence of these peaks after the incorporation of CQDs and NCQDs indicates that the long-range crystallinity and framework integrity of UiO-66 were preserved. CQDs and NCQDs interact mainly at the particle surfaces without disrupting the internal Zr-MOFs lattice. The average crystallite size decreased marginally from 63.21 nm for pristine UiO-66 to 60.61 nm (UiO-66/CQDs) and 58.74 nm (UiO-66/NCQDs), confirming stable framework integration.

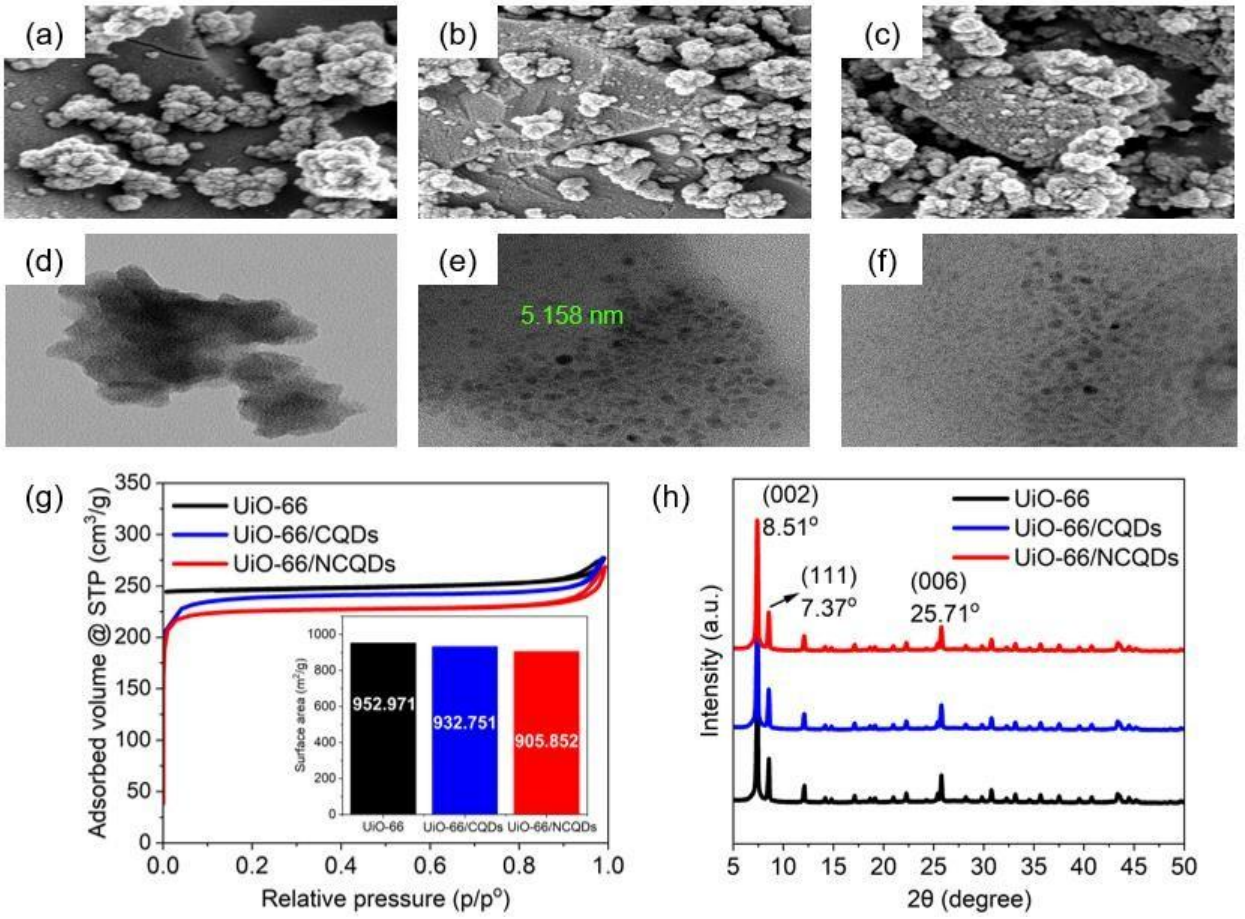


Fig. 3 FESEM (a–c) and TEM (d–f) micrographs of (a,d) pristine UiO-66, (b,e) UiO-66/CQDs, and (c,f) UiO-66/NCQDs nanocomposites, (g) $N_2$ adsorption–desorption isotherms with inset SBET comparison, and (h) XRD patterns showing structural integrity after CQDs and NCQDs incorporation

4.2 Interface bonding

The FTIR spectra of UiO-66, UiO-66/CQDs, and UiO-66/NCQDs were presented in Fig. 4(a) in the range of 4000–700 $cm^{-1}$ to identify the functional groups and bonding interactions in the composites. Pristine UiO-66 exhibited a broad O–H stretching band at 2800–3600 $cm^{-1}$, a C=O stretching of carboxylates at 1650–1580 $cm^{-1}$, hydroxyl bending at 1345 $cm^{-1}$, C–O stretching at 1153 $cm^{-1}$, and a Zr–O band at 842 $cm^{-1}$, confirming the coordination of BDC linkers to Zr–oxide

clusters and the integrity of the UiO-66 framework [22]. The UiO-66/CQDs exhibited C–H bending and C–O stretching at 1380–1300 $cm^{-1}$ and 1150–1085 $cm^{-1}$, respectively, indicating the successful integration of carbonaceous domains within the UiO-66 framework. New bands appeared in the UiO-66/NCQDs hybrid, corresponding to N–H bending (1640 $cm^{-1}$) and C–N stretching (1266 $cm^{-1}$), confirming the presence of nitrogen-containing functional groups derived from NCQDs [23]. The coexistence of abundant hydroxyl (–OH), carbonyl (–C=O), and nitrogen-containing groups on the CQDs/NCQDs and UiO-66 suggests favourable interfacial interactions dominated by hydrogen bonding and weak coordination between the functional groups on the surface of the QDs and the Zr nodes of the MOF [24], [25], as schematically illustrated in Fig. 5. Both UiO-66 and CQDs/NCQDs possess abundant oxygen-containing functional groups, particularly surface –OH moieties, which enhance surface polarity and wettability (Fig. S3). This favourable interfacial compatibility facilitates the intimate contact and uniform dispersion of the QDs on the UiO-66 framework, as evidenced by FESEM and TEM observations (Fig. 3(a-f)). The retention of the characteristic Zr–O and carboxylate (C=O) vibrational bands after nanocomposite formation confirms that the UiO-66 framework remained structurally intact. Meanwhile, the newly introduced surface functionalities enhanced interfacial compatibility and increased the accessible electroactive sites, which are beneficial for charge transfer and energy storage applications.

The $^{1}H$ NMR spectra of CQDs, NCQDs, UiO-66/CQDs and UiO-66/NCQDs (Fig. 4(b)) further corroborated the successful formation of UiO-66-based hybrid nanocomposites. The UiO-66/CQD and UiO-66/NCQD nanocomposites exhibited characteristic aromatic resonances at $\delta \approx$ 6.8 and 7.5–8.5 ppm, which were assigned to the phenyl protons of the terephthalate (BDC) ligands, confirming that the UiO-66 backbone remained structurally preserved after hybridisation. An additional resonance at $\delta \approx$ 2.3–2.6 ppm was observed in NCQDs and was retained in the UiO-66/NCQD composite; this resonance is attributable to methylene protons adjacent to primary amine groups ($–CH_2–NH_2$) derived from ethylenediamine. The persistence of this signal in the hybrid composites indicates that CQDs/NCQDs are anchored at the UiO-66 surface and defect sites. There, the QDs interact predominantly with the organic linkers and the UiO-66 surface through hydrogen bonding and π–π interactions, along with weak nitrogen coordination to Zr nodes, without compromising the integrity of the crystalline framework. Such interaction pathways are consistent with the proposed surface-coordination and pore-confinement mechanism schematically depicted in Fig. 5.

XPS was used to investigate the surface elemental composition and chemical-bonding states of UiO-66/CQDs and UiO-66/NCQDs. As shown in Fig. 4(c), the survey spectra confirmed the presence of Zr, C and O in both hybrids [26]. Furthermore, an additional N 1s signal was observed in the UiO-66/NCQD hybrid, confirming the successful incorporation of nitrogen-containing CQDs without introducing extraneous elements.

The high-resolution C 1s spectra (Fig. 4(d)) revealed the presence of C–C/C=C and C–O groups in the UiO-66/CQDs, originating from the UiO-66 organic linker and oxygenated functional groups of the CQDs. By contrast, UiO-66/NCQDs exhibited an additional C–N

contribution together with C–O and C=O/C=N species, indicating successful nitrogen functionalisation following NCQD incorporation. On the other hand, the O 1s spectra (Fig. 4(e)) showed contributions from the Zr–O bonds of the UiO-66 framework together with C–O and C=O groups associated with the QDs, indicating interfacial integration. The Zr 3d core-level spectra (Fig. 4(f)) consistently displayed the characteristic $Zr^{4+}$ spin-orbit doublet, confirming that the UiO-66 framework remained structurally intact after QD incorporation.

The high-resolution N 1s spectrum of UiO-66/NCQDs (Fig. 4(g)) was deconvoluted into two components centred at 398.65 and 400.12 eV, corresponding to pyridinic nitrogen (C–N) and pyrrolic nitrogen (N–H), respectively [27]. Table 2 presents the quantitative analysis of the fitted peak areas, revealing relative contributions of 57.76% pyridinic nitrogen and 42.24% pyrrolic nitrogen. The dominant pyridinic nitrogen content provides abundant electroactive sites and promotes surface redox reactions. By contrast, pyrrolic nitrogen improves electrolyte accessibility and facilitates ion transport. Therefore, the incorporation of nitrogen functionalities is likely to enhance charge-transfer kinetics and create a more favourable electrode–electrolyte interface, improving electrochemical behaviour in subsequent electrochemical evaluations.

Table 2. Quantitative analysis of N species obtained from N 1s XPS peak fitting for UiO-66/NCQDs

| N species | Binding energy (eV) | Relative content (%) |
|---|---|---|
| Pyridinic N | 398.65 | 57.76 |
| Pyrrolic N | 400.12 | 42.24 |

Overall, the XPS results confirm the successful integration of CQDs and NCQDs within the UiO-66 matrix through strong interfacial interactions while preserving the structural integrity of the UiO-66 framework.

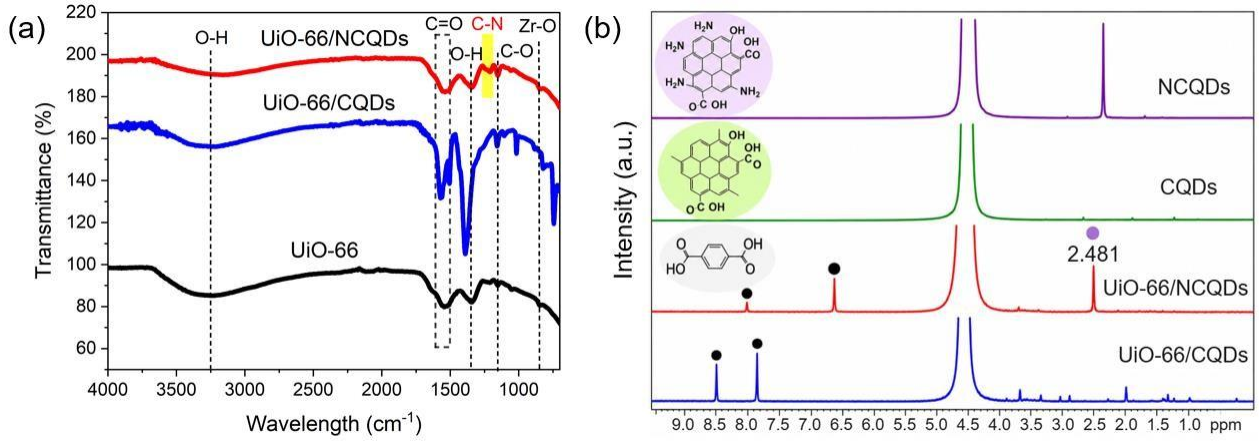

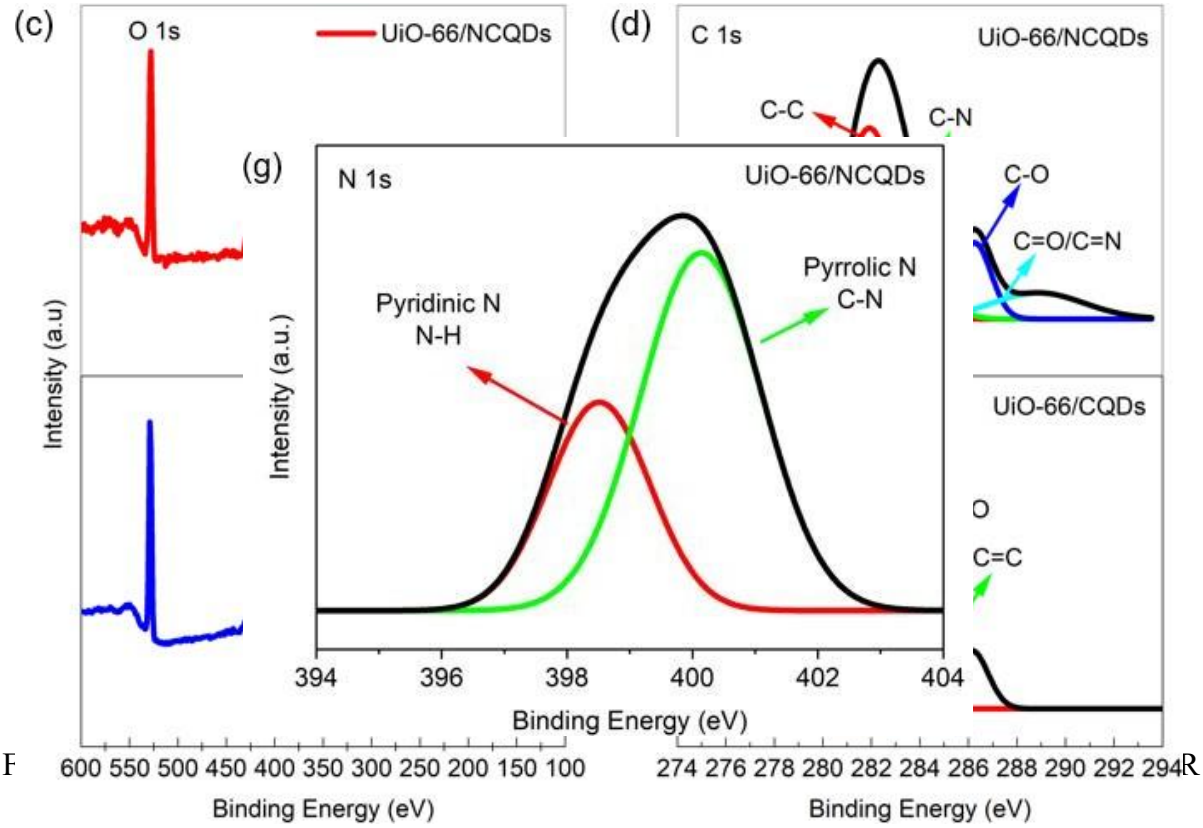


F R

66/CQDs and UiO-66/NCQDs, and high-resolution XPS spectra of (d) C 1s, (e) O 1s, (f) Zr 3d, and (g) N 1s regions for the hybrid nanocomposites

Fig. 5 schematically illustrates the structural framework of UiO-66 and the interaction mechanisms of CQDs and NCQDs within the UiO-66 host matrix. UiO-66 possesses a face-centered cubic (Fm-3m) topology constructed from $Zr_6O_4(OH)_4$ inorganic clusters coordinated with terephthalate organic linkers, forming interconnected tetrahedral and octahedral cages accessible through triangular windows.

As inferred from FTIR, $^1$H NMR, and XPS analyses, both CQDs and NCQDs interact with UiO-66 via surface anchoring and partial pore confinement. These interactions are governed by hydrogen bonding between the surface functional groups of the QDs (–OH, –COOH and –NH) and the Zr–O moieties of the UiO-66 framework, as well as π–π stacking between the graphitic domains of the QDs and the aromatic ring of the organic linkers.

The schematic highlights that CQDs are predominantly anchored on the external surface and near pore entrances, exhibiting limited penetration into the internal cages. By contrast, NCQDs exhibit greater pore confinement, facilitated by additional nitrogen-containing functionalities that enhance interfacial interactions with the UiO-66 framework. This enhanced confinement is consistent with the observed decrease in the BET surface area of the UiO-66/NCQDs, compared with UiO-66/CQDs.

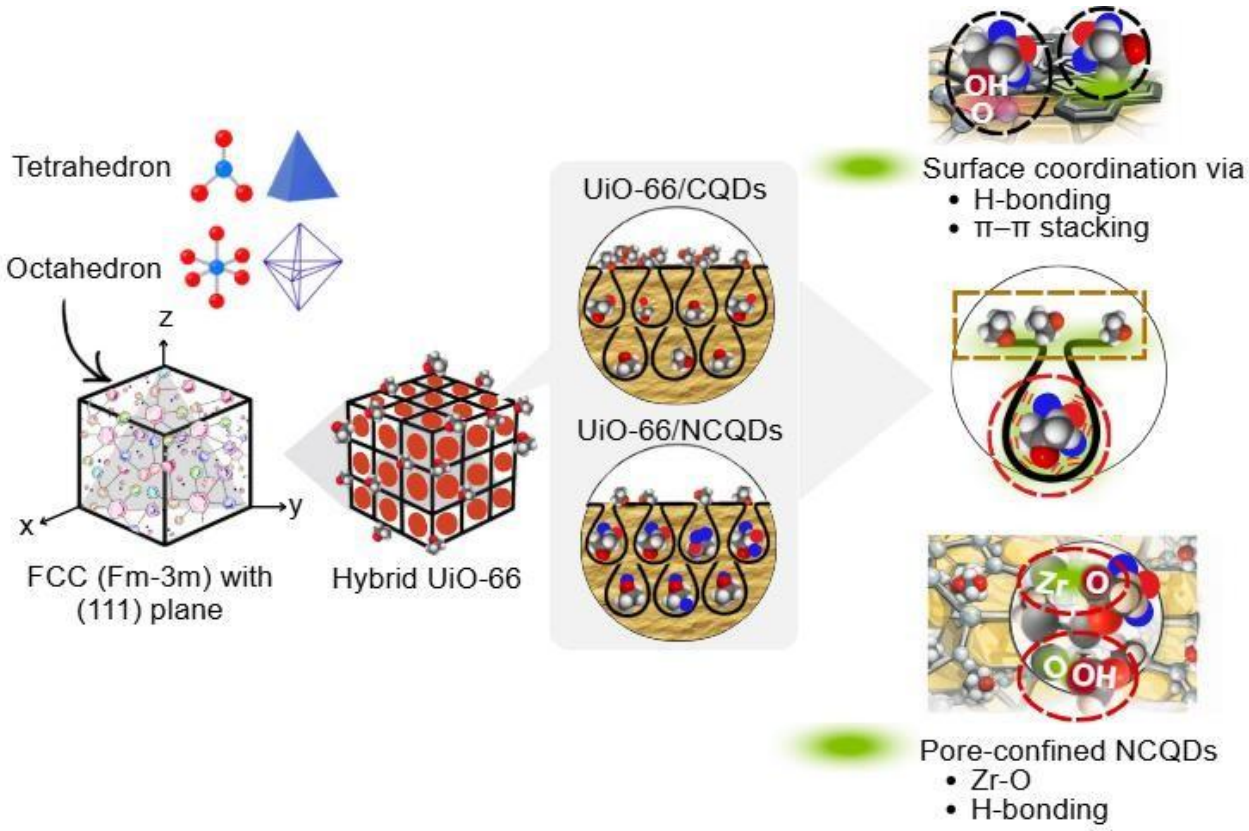


Fig. 5 Schematic illustration of the structural and interfacial interaction mechanisms of the hybrid UiO-66

### 4.2 Electrochemical Performance

#### 4.2.1 Three-Electrode System

EIS was used to examine ionic diffusion, bulk electrolyte characteristics, and electrode-electrolyte interface behaviour [28], [29], [30]. Nyquist plots derived from EIS measurements (Fig. 6(a)) in the frequency range $10^{-2}$ to $10^{5}$ Hz exhibited three distinct regions: (i) a high-frequency intercept corresponding to the equivalent series resistance ($R_s$), (ii) a suppressed mid-frequency semicircle associated with the charge-transfer resistance ($R_{ct}$) at the electrode/electrolyte interface, and (iii) a low-frequency inclined Warburg region related to ion diffusion and transport behaviour. Table 3 summarises the fitted resistance values. The $R_s$ values decreased from 0.923 Ω for UiO-66 to 0.662 Ω for UiO-66/CQDs and further to 0.608 Ω for UiO-66/NCQDs, indicating enhanced intrinsic conductivity after QD incorporation. The improvement was more pronounced for NCQDs, owing to their higher surface charge density, as evidenced by the more negative zeta potential (Fig. S4), which promoted interfacial interaction and dispersion within the UiO-66 framework. In addition, UV–Vis analysis and the corresponding Tauc plots (Fig. S5a–b) reveal a narrower optical band gap for NCQDs, likely due to nitrogen-induced defect states, which may contribute to enhanced electronic conductivity and interfacial charge-transfer characteristics [13]. Furthermore, photoluminescence (PL) analysis (Fig. S6) shows enhanced emission behaviour after

nitrogen incorporation, indicating modification of surface electronic states and suppression of non-radiative recombination pathways. These optical characteristics may facilitate charge transport and improve electrochemical kinetics. Similarly, the $R_{ct}$ values decreased from 8.063 Ω for pristine UiO-66 to 1.901 Ω (UiO-66/CQDs) and 1.635 Ω (UiO-66/NCQDs), indicating facilitated charge-transfer processes following hybridisation. Despite the reduced $R_s$ and $R_{ct}$ values, UiO-66/CQDs exhibited the highest transport resistance ($R_t$ = 18.05 Ω), suggesting hindered ion migration within the porous electrode network. This behaviour is associated with the lower colloidal stability and broader particle size distribution of CQDs compared to NCQDs, as supported by zeta potential analysis (Fig. S4) and previously reported TEM/DLS observations [13]. The reduced electrostatic repulsion in CQDs may promote localised aggregation, partially limiting electrolyte penetration and ion diffusion pathways. By contrast, UiO-66/NCQDs achieved the lowest $R_t$ value (11.81 Ω) and displayed the steeper low-frequency response, indicating improved diffusion kinetics and enhanced pseudocapacitive behaviour. Overall, the reduced resistance demonstrates that NCQDs act as efficient conductive nanodomains while maintaining accessible ion-transport pathways, consistent with the preserved porosity observed in the BET analysis (Fig. 3(g)).

Table 3 Fitted $R_s$, $R_{ct}$, and $R_t$ values extracted from Nyquist plot fitting of UiO-66, UiO-66/CQDs, and UiO-66/NCQDs

| Electrode | $R_s$ (Ω) | $R_{ct}$ (Ω) | $R_t$ (Ω) |
|---|---|---|---|
| UiO-66 | 0.923 | 8.063 | 14.43 |
| UiO-66/CQDs | 0.662 | 1.901 | 18.05 |
| UiO-66/NCQDs | 0.608 | 1.635 | 11.81 |

The CV profiles (Fig. 6(b)) of the UiO-66, UiO-66/CQDs, and UiO-66/NCQDs electrodes were recorded within a potential window of 0–0.6 V at a scan rate of 3 mV $s^{-1}$. All electrodes exhibited distinct redox peaks, confirming faradaic charge storage characteristics corresponding to a battery rather than capacitive mechanisms [31]. The anodic peak between 0.50–0.55 V is associated with $OH^-$ intercalation, whereas the cathodic peak between 0.30 and 0.45 V corresponds to de-intercalation. The UiO-66/NCQDs exhibited the largest enclosed CV area, 141.58% higher than that of UiO-66 and 25.61% higher than that of UiO-66/CQDs, indicating superior charge-storage capability. This enhancement is due to the synergistic role of NCQDs, which enhance electron transport pathways and reduce interfacial charge-transfer resistance [32]. The earlier oxidation onset of the UiO-66/NCQDs electrode reflects enhanced electron transfer over a broader potential window, yielding improved charge-transfer kinetics, specific capacity and reversibility.

Fig. 6(c) further investigates the CV response of UiO-66/NCQDs was recorded at varying scan rates from 3 to 50 mV $s^{-1}$. Both anodic and cathodic peaks shifted systematically, reflecting kinetic polarization due to diffusion constraints at higher sweep speeds [33]. This observation is consistent with the reduced $R_{bc}$ and $R_t$ values obtained from EIS (Fig. 6(a)), demonstrating the enhanced interfacial kinetics and ion accessibility within the NCQD-modified electrode. CV analysis revealed clear faradaic redox behaviour for all electrodes, with UiO-66/NCQDs exhibiting the largest enclosed area and enhanced peak currents. The improved redox activity and lower

polarisation confirm that NCQDs substantially boosted charge-transfer efficiency and overall electrochemical performance.

The GCD profiles (Fig. 6(d)) of the UiO-66 and its modified-MOFs electrodes were recorded within a potential window of 0–0.6 V at a current density of 1.0 A $g^{-1}$. The profiles exhibited non-linear and non-triangular characteristics, indicating the dominance of faradaic charge-storage processes rather than ideal EDLC behaviour [34], [35]. Among the investigated electrodes, UiO-66/NCQDs displayed the longest charge–discharge duration, reflecting its superior charge-storage capability and corroborating the redox activity observed in the CV curves (Fig. 6(b,c)). Furthermore, the corresponding internal resistance (iR) drops indicated 0.01925, 0.03588, and 0.01085 V for UiO-66, UiO-66/CQDs and UiO-66/NCQDs, respectively, implying that UiO-66/NCQDs exhibited the lowest internal resistance. By contrast, UiO-66/CQDs exhibited the highest iR drop, indicating inferior interfacial stability and less efficient electron transport, likely resulting from CQD agglomeration and non-uniform distribution on the UiO-66 surface. This observation is consistent with the EIS results (Fig. 6(a)), where UiO-66/NCQDs exhibited the smallest semicircle and lowest charge-transfer resistance.

Fig. 6(e) presents the GCD profiles of UiO-66/NCQDs were recorded at current densities ranging from 1.0–5.0 A $g^{-1}$. The nearly symmetric charge–discharge curves and preserved profile shapes evidence excellent electrochemical reversibility and structural stability during repeated charge-storage processes [31]. The specific capacitances derived from the GCD measurements are summarised in Fig. 6(f). At 1.0 A $g^{-1}$, UiO-66, UiO-66/CQDs, and UiO-66/NCQDs delivered specific capacitances of approximately 114, 174 and 290 C $g^{-1}$, respectively. When the current density increased to 5.0 A $g^{-1}$, the capacitance decreased to 39, 97 and 164 C $g^{-1}$, corresponding to capacitance retentions of 33.89%, 55.55% and 56.37%, respectively. The superior capacitance and rate capability of UiO-66/NCQDs indicate that the incorporation of nitrogen-doped CQDs enhanced charge-transfer kinetics, provided additional electroactive sites, and facilitated ion diffusion throughout the MOF framework. The enhanced electrochemical performance may be attributed to the pyridinic and pyrrolic nitrogen functionalities identified by XPS analysis (Fig. 4(g) and Table 2).

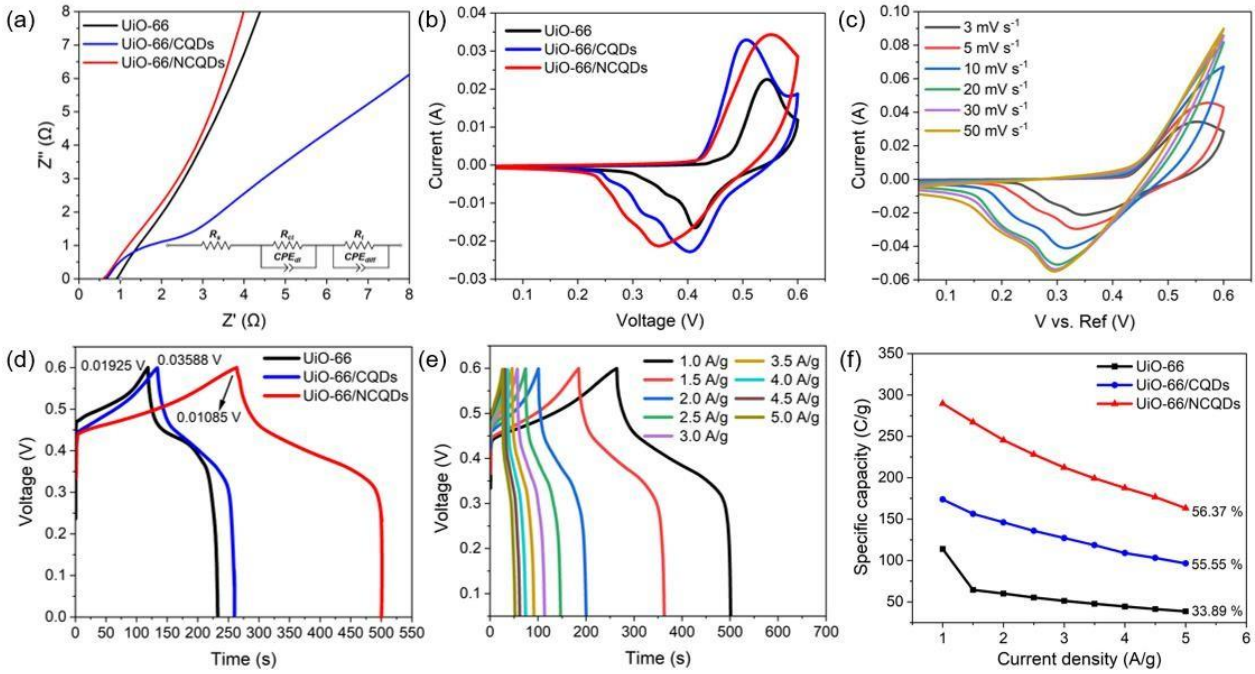


Fig. 6 (a) Nyquist plots with inset equivalent circuit model used for EIS fitting, (b) CV curves recorded within 0–0.6 V at a scan rate of 3 mV $s^{-1}$ and (c) at varying scan rates from 3 to 50 mV $s^{-1}$, (d) GCD profiles at a current density of 1.0 A $g^{-1}$ of UiO-66, UiO-66/CQDs, and UiO-66/NCQDs electrodes, (e) GCD curves of UiO-66/NCQDs at current densities ranging from 1.0 to 5.0 A $g^{-1}$, (f) Cycling stability showing capacity retention over prolonged charge-discharge cycles

### 4.2.2. Two-Electrode Device Evaluation

The CV curves of UiO-66/NCQDs//AC were recorded within various potential windows at a scan rate of 3 mV $s^{-1}$ in Fig. 7(a) to determine the optimum voltage window for the device. The voltage window is governed by the stability of the negative and positive electrodes of the device, where the AC anode typically operates up to 1.0 V and the UiO-66/NCQDs (cathode) up to 0.6 V, giving a theoretical maximum potential window of 1.6 V. The device remained stable up to 1.8 V; however, a sharp anodic peak appeared at 2.0 V with a reduced enclosed area under the curve, indicating electrolyte decomposition and instability.

Fig. 7(b) presents the CV profiles of the individual electrodes. The AC anode exhibited a nearly rectangular curve characteristic of electric double-layer capacitance. By contrast, the UiO-66/NCQDs cathode displayed distinct redox peaks associated with faradaic charge transfer. This complementary behaviour confirms the hybrid charge-storage mechanism of the assembled asymmetric supercapacitor.

CV curves of UiO-66/NCQDs//AC at scan rates ranging from 3 to 50 mV $s^{-1}$ within 0–1.8 V are shown in Fig. 7(c). The shapes of the curves remained almost unchanged as the scan rate increased, accompanied by a proportional increase in the current response. This stability

demonstrates high electrochemical reversibility and efficient ion diffusion, consistent with hybrid capacitor behaviour [36].

The GCD profiles (Fig. 7(d)) of UiO-66/NCQDs//AC were recorded within 0–1.8 V at current densities ranging from 1.0 to 5.0 A $g^{-1}$ The symmetrical charge–discharge curves confirmed the high reversibility of the device, consistent with the CV results (Fig. 7(c)), reflecting the coexistence of double-layer capacitive and faradaic reactions. The slight deviation from linearity indicates the presence of redox processes at the UiO-66/NCQD electrode (cathode), supporting the hybrid charge-storage mechanism. Notably, the iR drop remained minimal even at high current densities, suggesting efficient ion transport and low equivalent series resistance (ESR) (Fig. 6(a)). These observations highlight the ability of the device to maintain stable performance across a wide current density range.

Fig. 7(e) shows the cycling stability of the UiO-66/NCQDs//AC asymmetric device was evaluated over 8000 GCD cycles at a current density of 1 A $g^{-1}$ continuously without any rest periods to simulate rigorous practical operating conditions. An initial increase of 10.24% in capacitance within the first 1000 cycles was observed. This increase was attributed to electrode activation resulting from the penetration of electrolyte ions into the porous matrix and the establishment of stable ion-transport pathways. Despite pre-activation, extended cycling is required to fully expose electrochemically active sites and enhance ionic accessibility in MOF-based hybrid electrodes [37]. The device retained 83.87% of its initial capacitance after 7000 cycles, exceeding the reported 80.6 % capacity after 5000 cycles for MOF-derived supercapacitor electrodes [38]. This improved cycling stability can be attributed to the incorporation of NCQDs, which incorporate nitrogen-containing functional groups that enhance interfacial adhesion with the UiO-66 framework, facilitate charge transfer, and suppress structural degradation during repeated redox cycling. The observed capacitance fading with prolonged cycling is associated with progressive interfacial rearrangement or partial detachment of surface-anchored QDs under sustained electrochemical stress and thermal fluctuations.

Fig. 7(f) presents the Ragone plot of the UiO-66/NCQDs//AC asymmetric supercapacitor. The device delivered a maximum specific energy of 30.32 Wh $kg^{-1}$ at a corresponding specific power of 2449.38 W $kg^{-1}$ calculated based on the total mass of both electrodes. Thus, it demonstrated an exceptional capability to operate under high-power conditions while maintaining a competitive energy density. As summarised in Table 4, the specific energy of the UiO-66/NCQDs//AC is comparable to those of recently reported MOF- and carbon-based hybrid supercapacitors, including UiO-66//AC (29.6 Wh $kg^{-1}$) [39] and CQDs/NiCo-MOF//AC (30.61 Wh $kg^{-1}$) [40], while substantially exceeding those of ZIF-8 (9.04 Wh $kg^{-1}$) [41] and Cu-MOF//AC (3.39 Wh $kg^{-1}$) [42]. Although higher energy densities have been reported for Co–Ni MOF//AC (35.9 Wh $kg^{-1}$) [43], CrMoS@NiCo-MOF//AC (60.8 Wh $kg^{-1}$) [44], UiO-66/$MoS_2$//AC (66.87 Wh $kg^{-1}$) [45], and UiO-66/Se/PANI//AC (35.2 Wh $kg^{-1}$) [46], these systems operate at considerably lower specific powers ranging from 750 to 1280 W $kg^{-1}$. More importantly, the present UiO-66/NCQDs//AC device exhibits a remarkably high specific power of 2449.38 W $kg^{-1}$, far

exceeding those reported for UiO-66//AC (170 W $kg^{-1}$) [39], CQDs/NiCo-MOF//AC (620 W $kg^{-1}$) [40], ZIF-8 (350 W $kg^{-1}$) [41], Cu-MOF//AC (750 W $kg^{-1}$) [42], Co–Ni MOF//AC (750 W $kg^{-1}$) [43], CrMoS@NiCo-MOF//AC (1280 W $kg^{-1}$) [44], UiO-66/$MoS_2$//AC (1100 W $kg^{-1}$) [45] and UiO-66/Se/PANI//AC (977.02 W $kg^{-1}$) [46]. This outstanding power performance highlights the excellent rate capability and rapid charge–discharge characteristics of the UiO-66/NCQDs//AC system.

The enhanced electrochemical behaviour can be attributed to the incorporation of NCQDs within the UiO-66 framework, which improved electronic conductivity, facilitated interfacial charge transfer, and promoted efficient ion transport pathways. These effects are consistent with the reduced $R_{ct}$ fitted in the EIS spectra (Fig. 6(a)) and the highly reversible GCD profiles (Fig. 7(d)). From a practical perspective, the ability to maintain a moderate energy density while delivering an exceptionally high power output makes the UiO-66/NCQDs//AC device attractive for applications that require rapid energy delivery and fast charge–discharge operation. Therefore, incorporating NCQDs is an effective strategy for enhancing the high-rate electrochemical performance of UiO-66-based asymmetric supercapacitors.

Table 4 Comparison of the electrochemical performance of the UiO-66/NCQDs//AC asymmetric supercapacitor with recently reported UiO-66- and MOF-based hybrid supercapacitors

| Supercapacitor | Specific Energy (Wh $kg^{-1}$) | Specific Power (W $kg^{-1}$) | Ref |
|---|---|---|---|
| UiO-66//AC | 29.6 | 170 | [39] |
| CQDs/NiCo-MOF//AC | 30.61 | 620 | [40] |
| ZIF-8 | 9.04 | 350 | [41] |
| Cu-MOF//AC | 3.39 | 750 | [42] |
| Co-Ni MOF//AC | 35.9 | 750 | [43] |
| CrMoS@NiCo-MOF//AC | 60.8 | 1280 | [44] |
| UiO-66/$MoS_2$//AC | 66.87 | 1100 | [45] |
| UiO-66/Se/PANI//AC | 35.2 | 977.02 | [46] |
| UiO-66/NCQDs//AC | 30.32 | 2449.38 | |

Fig. 7(g) schematically illustrates the electrochemical characteristics derived from the CV, GCD, cycling stability, and Ragone plot analyses of the UiO-66/NCQDs//AC asymmetric supercapacitor. These results collectively indicate a hybrid charge-storage mechanism, in which electric double-layer capacitance (EDLC) is complemented by rapid and reversible interfacial pseudocapacitive reactions at the UiO-66/NCQDs positive electrode operating within a two-electrode aqueous device configuration.

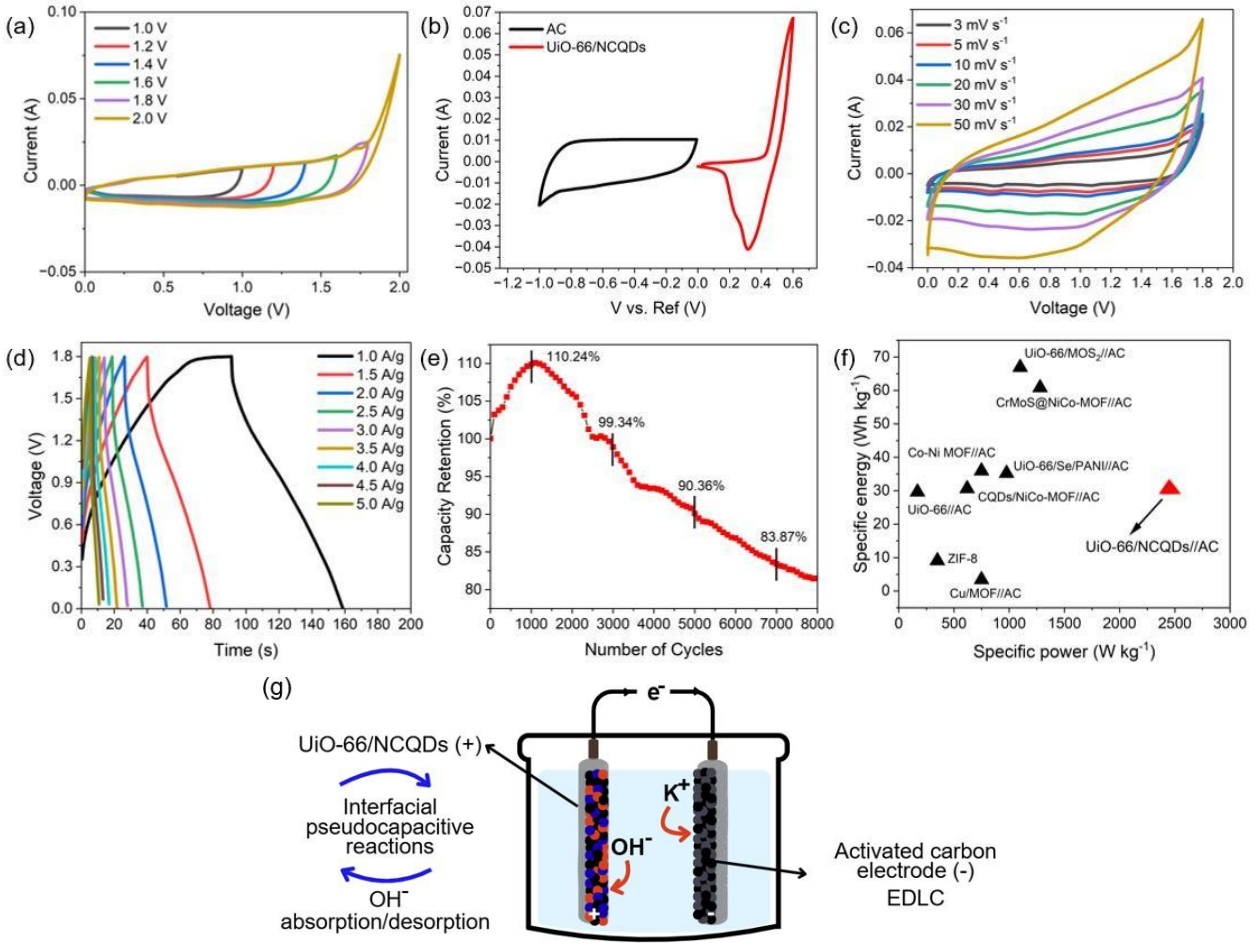


Fig. 7 (a) CV curves of the asymmetric UiO-66/NCQDs//AC device recorded at a scan rate of 3 mV $s^{-1}$ under different potential windows, (b) Individual CV curves of activated carbon (anode) and UiO-66/NCQDs (cathode), (c) CV curves at scan rates ranging from 3 to 50 mV $s^{-1}$, (d) GCD profiles at varying current densities, and (e) Cycling stability showing capacitance retention at 1 A $g^{-1}$, (f) Ragone plot comparing the energy and power densities of the UiO-66/NCQDs//AC asymmetric supercapacitor with previously reported carbon- and MOF-based hybrid devices, and (g) Schematic illustration of the charge-storage mechanism in the UiO-66/NCQDs//AC asymmetric supercapacitor

## 5.0 Conclusion

A sustainable and high-performance hybrid electrode for asymmetric supercapacitors (ASCs) was successfully developed in this study by embedding banana peel biomass-derived nitrogen-doped carbon quantum dots (NCQDs) into a UiO-66 framework. Structural analyses confirmed that the NCQDs were uniformly integrated, achieving a denser packing arrangement supported by strong H-bonding and Zr–O coordination without compromising the crystallinity of the MOF. Incorporating nitrogen-rich functional groups markedly improved pore confinement, interfacial compatibility, electrical conductivity and ion-diffusion kinetics. Therefore, the resulting UiO-66/NCQD hybrid exhibited superior specific capacitance, rate capability, and long-term

cycling stability, compared with pristine UiO-66. When assembled into an ASC device, the hybrid electrode delivered a highly competitive specific energy of 30.32 Wh $kg^{-1}$ and an outstanding specific power of 2449.38 W $kg^{-1}$, outperforming several previously reported MOF- and CQD-based systems. Ultimately, this work demonstrates a green, scalable pathway for engineering robust MOF/QD nanocomposites, offering a highly promising platform for advancing sustainable energy storage technologies.

## Declaration of competing interest

The authors declare that they have no known competing financial interests or personal relationships that could have influenced the work reported in this paper.

## Acknowledgements

The authors gratefully acknowledge the financial support from Universiti Kebangsaan Malaysia under the Research University Grant (GUP-2022-045) and the Ministry of Higher Education Malaysia through the Fundamental Research Grant Scheme (FRGS/1/2024/STG05/UKM/02/7). The authors also acknowledge the research facilities provided by Universiti Kebangsaan Malaysia and thank the technical staff for their assistance with experimental measurements.

## CRediT authorship contribution statement

Nur Irdina Atasya Abu Hassanisazin: Writing – original draft, Investigation, Data curation, Methodology, Visualization

Harivalagan Siva Kumar - Investigation, Formal analysis, Data curation, Methodology

Siti Aisyah Shamsudin: Funding Acquisition, Writing – review & editing, Supervision, Data curation, Conceptualization, Validation

Fatin Saiha Omar - Supervision

Theodore Azemtsop Manfo - Writing – review & editing

## Funding sources

This research was financially supported by Universiti Kebangsaan Malaysia through the Research University Grant (GUP-2022-045) and the Ministry of Higher Education Malaysia under the Fundamental Research Grant Scheme (FRGS/1/2024/STG05/UKM/02/7).

## References

[1] S. Anvari, A. Medina, R. P. Merchán, and A. C. Hernández, “Sustainable solar/biomass/energy storage hybridization for enhanced renewable energy integration in multi-generation systems: A comprehensive review,” Nov. 01, 2025, *Elsevier Ltd*. doi: 10.1016/j.rser.2025.115997.

[2] R. K. Azega *et al.*, “Supercapacitors and rechargeable batteries, a tale of two technologies: Past, present and beyond,” *Sustainable Materials and Technologies*, vol. 41, Sep. 2024, doi: 10.1016/j.susmat.2024.e01111.

[3] M. H. Waris *et al.*, “Composite electrode materials based on nickel cobalt sulfide/carbon nanotubes to enhance the Redox activity for high performance Asymmetric supercapacitor devices,” *Phys. Scr.*, vol. 98, no. 10, p. 105979, 2023, doi: 10.1088/1402-4896/acf52f.

[4] R. Atchudan, T. N. Jebakumar Immanuel Edison, M. Shanmugam, S. Perumal, T. Somanathan, and Y. R. Lee, “Sustainable synthesis of carbon quantum dots from banana peel waste using hydrothermal process for in vivo bioimaging,” *Physica E Low. Dimens. Syst. Nanostruct.*, vol. 126, Feb. 2021, doi: 10.1016/j.physe.2020.114417.

[5] K. Hagiwara *et al.*, “Role of alkan-1-ol solvents in the synthesis of yellow luminescent carbon quantum dots (CQDs): Van der Waals force-caused aggregation and agglomeration,” *RSC Adv.*, vol. 10, no. 24, pp. 14396–14402, Apr. 2020, doi: 10.1039/d0ra01349h.

[6] Y. Zheng, K. Chen, K. Jiang, F. Zhang, G. Zhu, and H. Xu, “Progress of synthetic strategies and properties of heteroatoms-doped (N, P, S, O) carbon materials for supercapacitors,” *J. Energy Storage*, vol. 56, p. 105995, Dec. 2022, doi: 10.1016/J.EST.2022.105995.

[7] T. Sruthi, M. Das, and V. Mathew, “First-principles investigation of nitrogen doping effects on the capacitance behavior of V2CTx MXenes,” *Physical Chemistry Chemical Physics*, vol. 27, no. 33, pp. 17376–17383, Aug. 2025, doi: 10.1039/d5cp01703c.

[8] V. Packirisamy, R. Ariyamuthu, K. Thangavelu, V. V. Murugesan, and J. Rugmangathan, “Banana peel biomass–derived activated carbon for nickel ion removal and energy storage applications,” *Biomass Convers. Biorefin.*, 2025, doi: 10.1007/s13399-025-06703-5.

[9] M. K. Muthukumaran *et al.*, “Recent advances in metal-organic frameworks for electrochemical sensing applications,” Aug. 01, 2025, *Elsevier B.V.* doi: 10.1016/j.talo.2024.100396.

[10] J. Winarta *et al.*, “A Decade of UiO-66 Research: A Historic Review of Dynamic Structure, Synthesis Mechanisms, and Characterization Techniques of an Archetypal Metal-Organic Framework,” *Cryst. Growth Des.*, vol. 20, no. 2, pp. 1347–1362, Feb. 2020, doi: 10.1021/acs.cgd.9b00955.

[11] T. Tang *et al.*, “Improving the surface area of metal organic framework-derived porous carbon through constructing inner support by compatible graphene quantum dots,” *J. Colloid Interface Sci.*, vol. 623, pp. 77–85, Oct. 2022, doi: 10.1016/J.JCIS.2022.04.161.

[12] R. Zhao *et al.*, “Carbon quantum dots/UiO-66@polysulfone porous microspheres fabricated via pickering emulsion template for pollutant removal,” *Sep. Purif. Technol.*, vol. 337, p. 126367, Jun. 2024, doi: 10.1016/J.SEPPUR.2024.126367.

[13] H. Siva Kumar, S. A. Shamsudin, M. N. Bin, and A. Azian, "Optimized Nitrogen-Doping of Carbon Quantum Dots from Banana Peel Waste: A Highly Selective Fe 2+ Sensor Probe," *Diam. Relat. Mater.*, 2024, doi: https://doi.org/10.1016/j.diamond.2024.111351.

[14] Y. L. Wang, S. Zhang, Y. F. Zhao, J. Bedia, J. J. Rodriguez, and C. Belver, "UiO-66-based metal organic frameworks for the photodegradation of acetaminophen under simulated solar irradiation," *J. Environ. Chem. Eng.*, vol. 9, no. 5, Oct. 2021, doi: 10.1016/j.jece.2021.106087.

[15] P. Naskar, P. Chakraborty, D. Kundu, A. Maiti, B. Biswas, and A. Banerjee, "Envisaging Future Energy Storage Materials for Supercapacitors: An Ensemble of Preliminary Attempts," Feb. 04, 2021, *Wiley-Blackwell*. doi: 10.1002/slct.202100049.

[16] V. V. Butova *et al.*, "Photoswitchable zirconium mof for light-driven hydrogen storage," *Polymers (Basel).*, vol. 13, no. 22, Nov. 2021, doi: 10.3390/polym13224052.

[17] T. Balakrishnan, W. L. Ang, E. Mahmoudi, and N. S. Sambudi, "Recent development of quantum dots@metal-organic framework composites as potential chemical and biological luminescence nanosensors," *Physica B Condens. Matter*, vol. 673, Jan. 2024, doi: 10.1016/j.physb.2023.415485.

[18] S. K. Gebremariam *et al.*, "MOF@MOF core-shell hybrid adsorbents with controlled water vapor affinity towards enhanced and steady CO2 capture in moist conditions," *Carbon Capture Science and Technology*, vol. 14, Mar. 2025, doi: 10.1016/j.ccst.2024.100356.

[19] R. M. Rego, G. Sriram, K. V. Ajeya, H. Y. Jung, M. D. Kurkuri, and M. Kigga, "Cerium based UiO-66 MOF as a multipollutant adsorbent for universal water purification," *J. Hazard. Mater.*, vol. 416, p. 125941, Aug. 2021, doi: 10.1016/J.JHAZMAT.2021.125941.

[20] R. M. Rego, M. D. Kurkuri, and M. Kigga, "A comprehensive review on water remediation using UiO-66 MOFs and their derivatives," *Chemosphere*, vol. 302, p. 134845, Sep. 2022, doi: 10.1016/J.CHEMOSPHERE.2022.134845.

[21] Z. Lu and X. Ren, "Pseudocapacitive Storage in High-Performance Flexible Batteries and Supercapacitors," Feb. 01, 2025, *Multidisciplinary Digital Publishing Institute (MDPI)*. doi: 10.3390/batteries11020063.

[22] K. L. Timofeev, S. A. Kulinich, and T. S. Kharlamova, "NH2-Modified UiO-66: Structural Characteristics and Functional Properties," *Molecules*, vol. 28, no. 9, May 2023, doi: 10.3390/molecules28093916.

[23] K. G. Nguyen *et al.*, "Investigating the effect of N-doping on carbon quantum dots structure, optical properties and metal ion screening," *Sci. Rep.*, vol. 12, no. 1, Dec. 2022, doi: 10.1038/s41598-022-16893-x.

[24] N. A. Mahat and S. A. Shamsudin, “Transformation of oil palm biomass to optical carbon quantum dots by carbonisation-activation and low temperature hydrothermal processes,” *Diam. Relat. Mater.*, vol. 102, Feb. 2020, doi: 10.1016/j.diamond.2019.107660.

[25] S. Šafranko *et al.*, “Preparation of multifunctional n-doped carbon quantum dots from citrus clementina peel: Investigating targeted pharmacological activities and the potential application for fe3+ sensing,” *Pharmaceuticals*, vol. 14, no. 9, Sep. 2021, doi: 10.3390/ph14090857.

[26] S. Chen *et al.*, “Development of a Zr-Based Metal-Organic Framework (UiO-66) for a Cooperative Flame Retardant in the PC/ABS,” *Polymers (Basel).*, vol. 16, no. 14, Jul. 2024, doi: 10.3390/polym16142083.

[27] D. Sengottuvelu *et al.*, “Multicolor Nitrogen-Doped Carbon Quantum Dots for Environment-Dependent Emission Tuning,” *ACS Omega*, vol. 7, no. 31, pp. 27742–27754, Aug. 2022, doi: 10.1021/acsomega.2c03912.

[28] Theodore Azemtsop Manfo, Mustafa Ergin Şahin, and Derya Bal Altuntaş, “Development of quasi-flexible solid polymer blend electrolytes and boron carbide reinforced tea waste electrodes for supercapacitors,” *J. Energy Storage*, pp. 1–13, Mar. 2025.

[29] M. T. Azemtsop, R. M. Mehra, Y. Kumar, and M. Gupta, “Physical Characterization of Ionic Liquid-Modified Polyvinyl Alcohol and Sodium Thiocyanate Polymer Electrolytes for Electrochemical Double-Layer Capacitor Application,” *J. Shanghai Jiaotong Univ. Sci.*, vol. 28, no. 2, pp. 161–171, Apr. 2023, doi: 10.1007/s12204-021-2397-y.

[30] T. Azemtsop Manfo, “Development and Characterization of a New Solid Polymer Electrolyte for Supercapacitor Device,” *International Journal of Electrochemistry*, vol. 2023, pp. 1–15, Oct. 2023, doi: 10.1155/2023/4825624.

[31] M. Z. Iqbal *et al.*, “Exploring MOF-199 composites as redox-active materials for hybrid battery-supercapacitor devices,” *RSC Adv.*, vol. 13, no. 5, pp. 2860–2870, Jan. 2023, doi: 10.1039/d2ra06457j.

[32] R. D. Septianto, L. Liu, F. Iskandar, N. Matsushita, Y. Iwasa, and S. Z. Bisri, “On-demand tuning of charge accumulation and carrier mobility in quantum dot solids for electron transport and energy storage devices,” *NPG Asia Mater.*, vol. 12, no. 1, Dec. 2020, doi: 10.1038/s41427-020-0215-x.

[33] L. Yaqoob, T. Noor, and N. Iqbal, “An overview of supercapacitors electrode materials based on metal organic frameworks and future perspectives,” Mar. 25, 2022, *John Wiley and Sons Ltd*. doi: 10.1002/er.7491.

[34] M. Liang *et al.*, “Carbon Quantum Dots-Modulated Interfacial Charge Transfer between Highly Nitrogen-Doped Tubular-Like Carbon and Cobalt Molybdate for Surface-Capacitive

Sodium-Ion Seizing," *ACS Sustain. Chem. Eng.*, vol. 13, no. 34, pp. 13929–13939, Sep. 2025, doi: 10.1021/acssuschemeng.5c04805.

[35] M. B. Idris, B. B. Mamba, and F. Xolile, "Understanding the charge-storage mechanism and interfacial kinetics of graphitic carbon nitride electrodes in redox-additive electrolytes for supercapacitors," *RSC Adv.*, vol. 16, no. 1, pp. 246–260, 2026, doi: 10.1039/d5ra09074a.

[36] C. Cougnon, "Impact of the Scan Rate on the Stability Window of an Electrical Double-Layer Capacitor," *Energies (Basel).*, vol. 16, no. 15, Aug. 2023, doi: 10.3390/en16155687.

[37] J. Olchowka *et al.*, "Stabilization and Improvement of Energy Storage Performance of High Mass Loading Cobalt Hydroxide Electrode by Surface Functionalization," *J. Electrochem. Soc.*, vol. 167, no. 10, p. 100527, Jun. 2020, doi: 10.1149/1945-7111/ab9a03.

[38] M. Y. Khan *et al.*, "Enhanced pseudocapacitive performance of a Pb-based MOF/FCNT composite for high-stability supercapacitor applications: a step ahead towards energy storage," *Dalton Transactions*, vol. 55, no. 1, pp. 215–237, 2026, doi: 10.1039/D5DT02586A.

[39] A. Kaur, V. Shrivastav, P. Dubey, I. Mudahar, S. Sundriyal, and S. Mishra, "Surface and Diffusion Characteristics of Nanoporous UiO-66/Pineapple Peel-Derived Carbon Composites for Solid-State Supercapacitors," *ACS Appl. Nano Mater.*, vol. 7, no. 16, pp. 18115–18127, Aug. 2024, doi: 10.1021/acsanm.3c01897.

[40] R. Kumari, M. Prajapati, and C. Ravi Kant, "NiCo MOF@Carbon Quantum Dots Anode with Soot Derived Activated Carbon Cathode: An Efficient Asymmetric Configuration for Sustainable High-Performance Supercapacitors," *Adv. Sustain. Syst.*, vol. 8, no. 10, Oct. 2024, doi: 10.1002/adsu.202400109.

[41] J. Wu, X. Zhang, F. Wei, Y. Sui, and J. Qi, "Controllable synthesis of ZIF-derived nano-hexahedron porous carbon for supercapacitor electrodes," *Mater. Lett.*, vol. 258, p. 126761, Jan. 2020, doi: 10.1016/J.MATLET.2019.126761.

[42] Z. Salehi Rozveh, M. Pooriraj, M. Rad, V. Safarifard, and M. Moradi, "Synergistic effect of metal node engineering and mixed-linker-architected on the energy storage activities of pillar-layered Cu2(L)2(DABCO) metal-organic frameworks," *Mater. Chem. Phys.*, vol. 292, p. 126761, Dec. 2022, doi: 10.1016/J.MATCHEMPHYS.2022.126761.

[43] S. Wang *et al.*, "Tunable architecture of cobalt-nickel metal-organic framework/activated carbon composites for superior electrochemical performance in asymmetric supercapacitors," *J. Colloid Interface Sci.*, vol. 684, pp. 647–657, Apr. 2025, doi: 10.1016/J.JCIS.2025.01.002.

[44] A. S. Alqarni *et al.*, "Interface Engineering of CrMoS@NiCo-MOF Nanocomposite and Sustainable Green Activated Carbon for Energy Storage and Hydrogen Production," *J.*

*Inorg. Organomet. Polym. Mater.*, vol. 35, no. 10, pp. 8648–8666, Oct. 2025, doi: 10.1007/s10904-025-03764-x.

[45] B. M. Raffah, H. Hassan, M. W. Iqbal, Y. Al-Hadeethi, and B. Arkook, "'Novel UiO-66/MoS2 hybrid materials: Dual-functionality as battery/supercapacitor electrodes and electrocatalysts for HER,'" *J. Energy Storage*, vol. 106, p. 114881, Jan. 2025, doi: 10.1016/J.EST.2024.114881.

[46] R. M. Nageib, S. G. Mohamed, M. Gaber, R. M. Salm, A. A. EL Amin, and X. Li, "Unveiling the Aqueous Battery-Type Energy Storage Systems Through UiO-66/Se/PANI Composite," *J. Inorg. Organomet. Polym. Mater.*, vol. 35, no. 4, pp. 2792–2813, Apr. 2025, doi: 10.1007/s10904-024-03426-4.

**Supplementary Data**

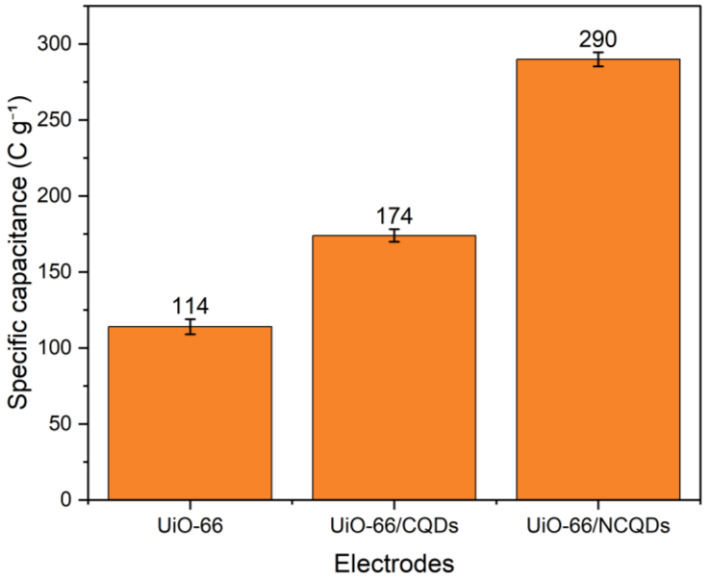


Fig. S1. Specific capacitance of UiO-66, UiO-66/CQDs, and UiO-66/NCQDs electrodes measured at 1.0 A $g^{-1}$. Error bars represent the standard deviation from three independently prepared electrodes (n = 3)

Table S1. Triplicate specific capacitance values of UiO-66, UiO-66/CQDs, and UiO-66/NCQDs electrodes at 1.0 A $g^{-1}$

| Electrodes | Rep 1 | Rep 2 | Rep 3 | Average ± SD |
|---|---|---|---|---|
| UiO-66 | 108.0 | 114.5 | 119.5 | 114.0 ± 5.8 |
| UiO-66/CQDs | 170.2 | 178.4 | 173.4 | 174.0 ± 4.1 |
| UiO-66/NCQDs | 285.7 | 294.9 | 289.4 | 290.0 ± 4.6 |

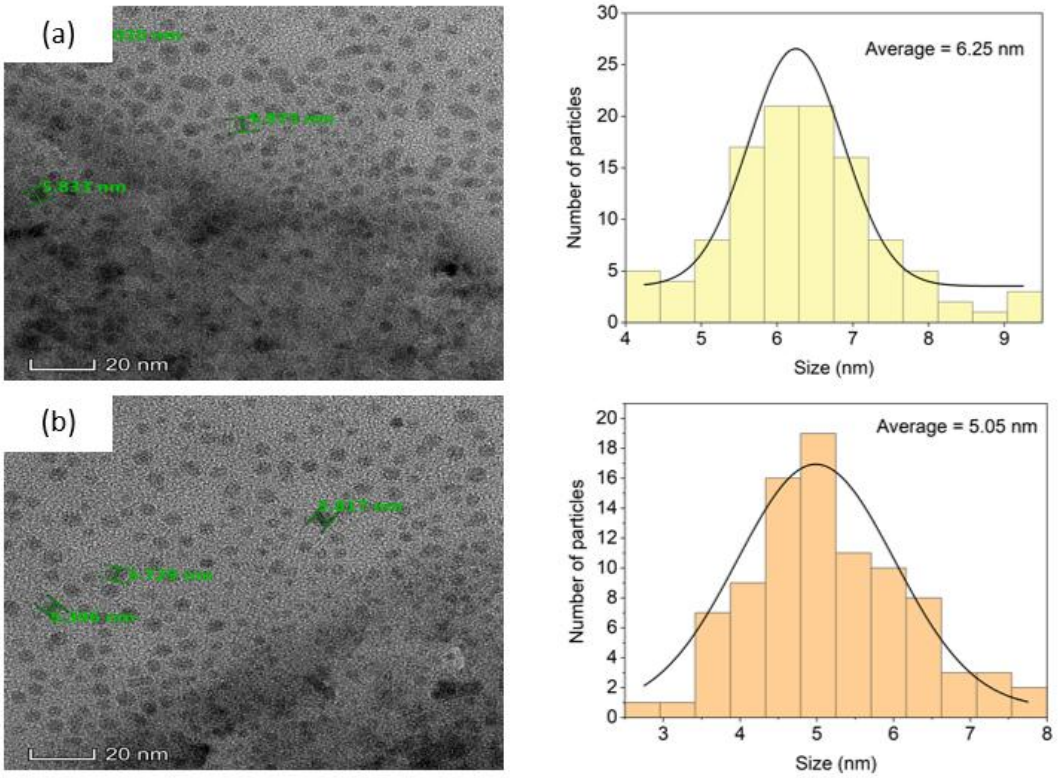


Fig. S2 TEM images and corresponding particle size distribution histograms of (a) CQDs and (b) NCQDs

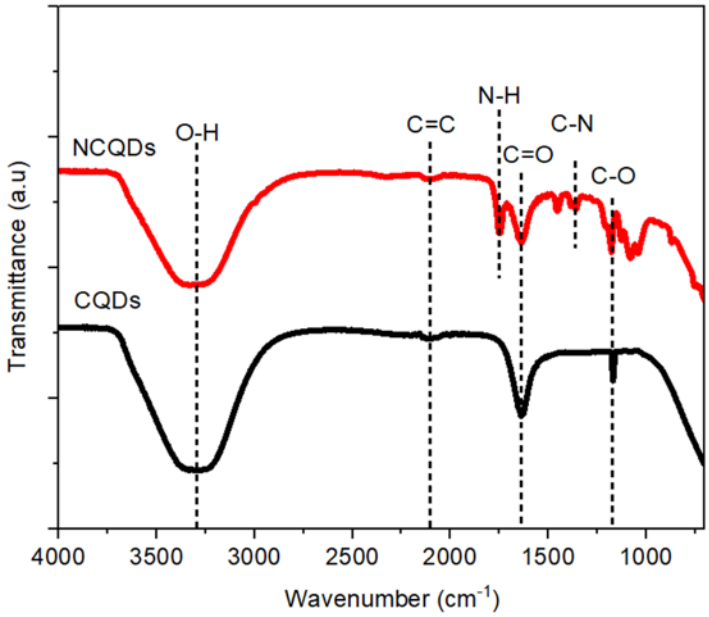


Fig. S3 FTIR spectra of pristine CQDs and NCQDs showing the presence of O–H, C=O, C–O, and C–N functional groups

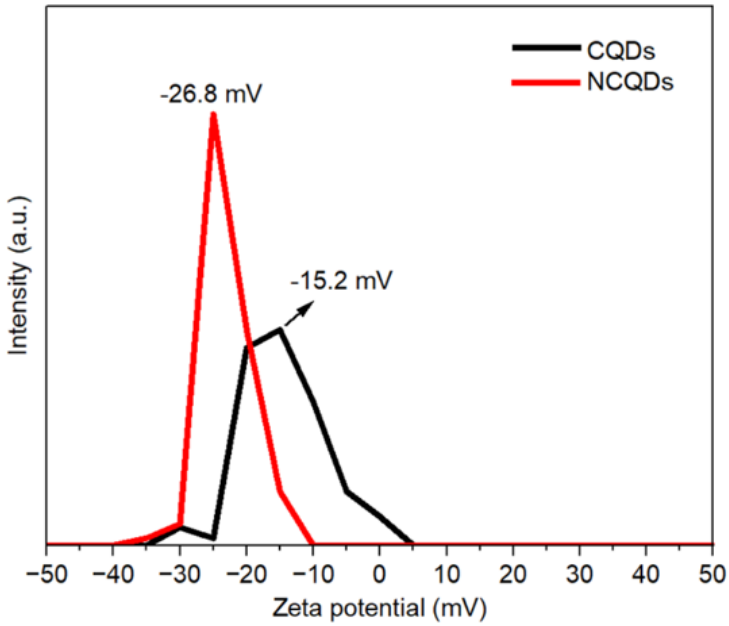


Fig. S4 Zeta potential distributions of CQDs and NCQDs showing differences in surface charge characteristics

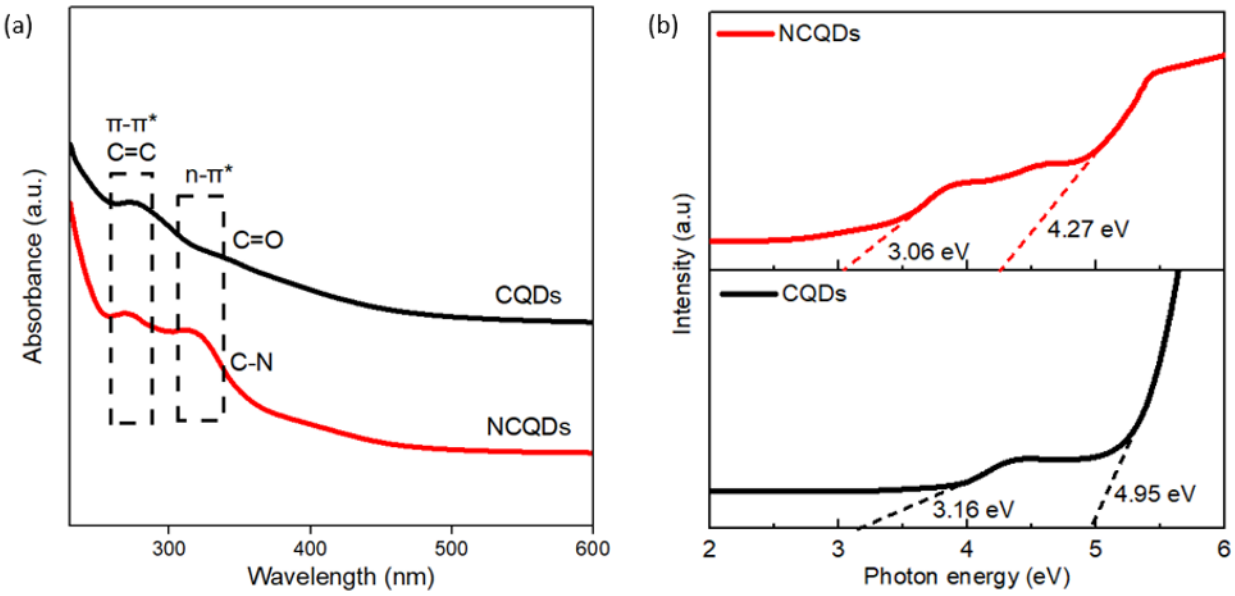


Fig. S5 (a) UV–Vis absorption spectra and (b) corresponding Tauc plots of CQDs and NCQDs, showing the reduced optical band gap after nitrogen doping

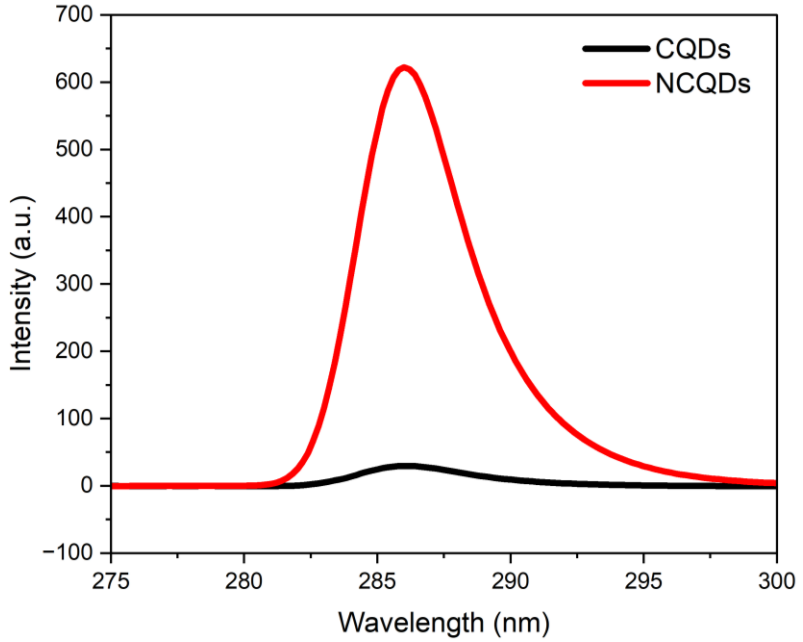


Fig. S6 Photoluminescence (PL) emission spectra of CQDs and NCQDs demonstrating the effect of nitrogen incorporation on optical emission behavior